DOI: 10.1002/ejic.200501093

In Search of Binary Hybrid Systems in Manganese Chemistry: The Synthesis, Spectroscopic and Structural Characterization, and Magnetic Properties of a New Species in the Aqueous Mn^{II}-Quinic System

Melita Menelaou,[a] Catherine P. Raptopoulou,[b] Aris Terzis,[b] Vassilis Tangoulis,[c] and Athanasios Salifoglou*[a]

Keywords: Manganese / Structural speciation / Mn^{II}–quinate interactions / Magnetic properties / Hybrid materials

Manganese is a metal with diverse (bio)chemical reactivity in aqueous media in the presence of biologically relevant ligands. Key to that reactivity is the existence of soluble and bioavailable forms of Mn^{II} across the physiological range of pH. To probe the interactions arising between Mn^{II} and the low-molecular-mass ligand D-(–)-quinic acid, research efforts were targeted at the synthetic aqueous chemistry in the requisite binary system. The pH-specific synthetic reaction of Mn^{II} with D-(–)-quinic acid led to the isolation of the new species $[Mn_2(C_7H_{11}O_6)_4]_n{\cdot}nH_2O$ (**1**). Complex **1** was characterized by elemental analysis, spectroscopic techniques (EPR, FTIR), thermal and magnetic studies, and X-ray crystallography. The molecular lattice of **1** reveals the presence of dimeric units of Mn^{II} centers, with the quinate ligands coordinated to the metal ions through variable binding modes, indicating the diversity of chemical reactivity in the system. The octahedral Mn^{II} centers in the molecular assembly of **1** serve as chemical prototypes of the forms of interactions that most likely develop in biologically relevant fluids, similar to those encountered in plant exudates and plant cellular structures. Concurrently, the physicochemical features of **1** (from the 3D hydrogen-bonding network to the magnetic susceptibility properties and EPR spectral results) exemplify the key features that constitute the rudiments of Mn^{II}-organic hybrid lattices of specific functions and (bio)chemical reactivity patterns. The collective properties of **1** are discussed in the context of their occurrence in natural binary Mn^{II}-influenced systems and advanced metal-hybrid materials of potential applications.

Introduction

Manganese is an element of considerable occurrence in the earth's lithosphere. It is found in minerals as well as biological systems. In the biotic systems, manganese is an essential element[1] and is involved in the active sites of metalloenzymes, key to the integrity of cellular processes.[2] Among those are catalases,[3] the mitochondrial superoxide dismutase (SOD) and pyruvate carboxylase, the glial-specific enzyme glutamine synthetase, and others.[4] Albeit controversial, the role of manganese in cellular processes in the brain has been the subject of considerable research, given that the specific metal in its ionic forms can cross the blood brain barrier and behave as a neurotoxin.[5] As a result, manganese ions and their chemical reactivity have been associated with physiological aberrations in humans, including manganism and a number of other neurological impairments such as Parkinson's disease. Outstanding, on the other hand, is the participation of manganese in the oxygen-evolving complex of photosystem II (PSII), with the manganese playing an important role as an inorganic cofactor of catalytic importance.[6]

Metal ions in biological systems are mobilized efficiently through interactions with organic substrates, that is, ligands capable of coordinating them and solubilizing them in biological fluids. These ligands include both low- and high-molecular-mass cellular targets. Manganese, as Mn^{II} and/or Mn^{III}, aptly coordinates to such ligands and enters further ternary interactions with biological molecules. One such low-molecular-mass molecule is D-(–)-quinic acid, 1α,3α,4α,5β-tetrahydroxy-1-cyclohexane carboxylic acid. It is a molecule that is found widely in plants where it is a precursor to shikimic acid.[7] The latter molecule is involved in the synthesis of essential amino acids. Hence, the presence of quinic acid appears to be vital to cellular physiology,[7a,8] with the organic acid capable of binding metal ions in biological fluids. Among the metal-ion nutrients targeted by such ligands are $Fe^{II,III}$, Mn^{II}, Zn^{II}, Cu^{II}, and others. In exemplifying its chemical reactivity towards Mn^{II}, quinic acid contains three very important features that render it

---

[a] Department of Chemical Engineering, Aristotle University of Thessaloniki, Thessaloniki 54124 and Chemical Process Engineering Research Institute,
Thermi, Thessaloniki 57001, Greece
Fax: +30-2310-996-196
E-mail: salif@auth.gr
[b] Institute of Materials Science, NCSR "Demokritos",
Aghia Paraskevi 15310, Attiki, Greece
[c] Department of Materials Science, University of Patras,
Patras 26500, Greece

an efficient metal-ion binder. It contains (a) a carboxylate moiety known to promote binding, (b) alcohol moieties, one of which is in an α position to the carboxylate group, and (c) three alcohol groups relevant to polyol functionalities. In all cases, coordination to a metal ion like Mn^{II} promotes solubilization and contributes to Mn^{II} bioavailability, leading to metallo(bio)chemical interactions characterizing the role of the specific metal ion in cellular environments like those of a plant.

On the basis of these views, the exploration of the aqueous chemistry of Mn^{II} with α-hydroxycarboxylate binders, like D-(–)-quinic acid, is expected to (a) shed light on the structural speciation of that aqueous binary system and (b) provide chemical clues on the interaction of that metal ion with a biologically important substrate, the reactivity of which plays an important role in cellular biosynthetic pathways. The paucity of related Mn^{II}-quinic acid derivative species prompted us to look into the pH-specific synthetic chemistry of that binary system. To this end, we herein report on (a) the synthesis and spectroscopic properties of a new Mn^{II}-quinate species $[Mn_2(C_7H_{11}O_6)_4]_n{\cdot}nH_2O$ (**1**) and (b) the relevance of the physicochemical properties of **1** in the development of interactions of Mn^{II} with biologically relevant targets and the assembly of lattices illustrating the solid-state features of multimodal quinate-containing Mn^{II} materials.

Results and Discussion

Synthesis

A simple procedure was employed for the synthesis of **1**. A facile reaction between Mn^{II} and quinic acid in aqueous media occurred at pH 3. The pH was adjusted to 3 by addition of aqueous ammonia. The stoichiometric reaction that led to the formation of compound **1** is shown by Reaction 1.

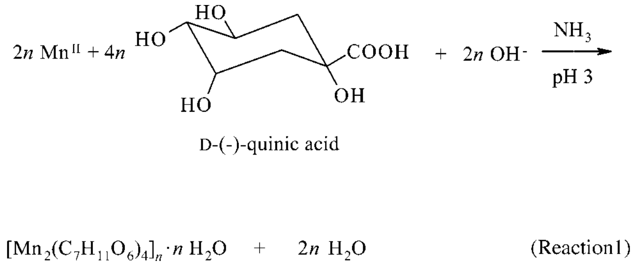

The derived hybrid Mn^{II}-quinate material was easily retrieved in pure crystalline form upon standing of the reaction mixture at room temperature and allowing for slow evaporation over a period of 24 to 36 hours. Elemental analysis of the isolated colorless crystalline product indicated the molecular formulation $[Mn_2(C_7H_{11}O_6)_4]{\cdot}H_2O$. Further evaluation of the crystalline product by FTIR spectroscopy confirmed the presence of quinate bound to Mn^{II}, consistent with the proposed formulation. Finally, X-ray crystallography confirmed the analytical and spectroscopic results by rendering the molecular formulation of the crystalline product as $[Mn_2(C_7H_{11}O_6)_4]_n{\cdot}nH_2O$ (**1**). In a synthetic effort making use of various bases, the same reaction mixture of Mn^{II} and quinic acid reacted in the presence of NaOH and KOH to a final pH value of 3, finally affording a crystalline solid. That solid proved to be complex **1** by virtue of its identical FTIR spectrum with that of the title compound beyond the elemental analysis results. Attempts to synthesize a congener Mn^{III}-quinate species in aqueous solutions under identical conditions to Reaction 1 [using M^{III}(acetate)$_3$ and quinic acid with a molecular ratio 1:2 in the presence of ammonia] consistently led to the isolation of a Mn^{II} species, which was shown to be **1** by spectroscopic and crystallographic methods. Other reaction conditions leading to Mn^{III} species of quinate are currently being investigated.

Compound **1** is insoluble in water. It is also insoluble in organic solvents like methanol, acetonitrile, chlorinated solvents ($CHCl_3$, CH_2Cl_2), toluene, and DMF. Complex **1** is stable in the crystalline form in the air at room temperature for long periods of time.

Description of the Crystal Structure

Compound **1** emerges from a molecular type of crystal lattice. The ORTEP diagram for complex **1** is shown in Figure 1. Selected bond lengths and angles for **1** are given in Table 1. Complex **1** crystallizes in the monoclinic space group $P2_1$ with two molecules per unit cell. In complex **1**, there are two distinct types of Mn^{II} ions, with each residing in a variable-nature coordination environment. In the first type of Mn^{II} ions, reflected in the $Mn1^{II}$ assembly, one quinate ligand coordinates to the metal ion through the carboxylate and alcohol oxygens O1 and O3, respectively. These two moieties bind to Mn^{II} through the formation of a five-membered metallacyclic ring, rendering the arising species quite stable. The second carboxylate oxygen atom, O2, of that quinate ligand coordinates to a neighboring Mn1′ ion [(′): 1 + *x*, *y*, *z*] leading to the *syn-anti* bridging mode of the carboxylate moiety depicted as mode I in Scheme 1. The interatomic distance between the so bridged Mn^{II} ions (Mn1 and Mn1′) is evidently equal to the length of the *a* crystallographic axis [5.813(3) Å]. This type of bridging is responsible for the formation of chains of Mn1 assemblies along the *a* axis (Figure 2). A second quinate ligand entering the coordination sphere of the Mn1 ion employs a similar coordination mode by using one of the carboxylate and the alcohol oxygen atoms to anchor to Mn1 (O11 and O13, respectively). The second terminal oxygen, O12, of the carboxylate group, however, does not participate in the coordination of an adjacent manganese ion as was the case with the first quinate ligand. Thus, the carboxylate group of the second quinate ligand adopts the monodentate coordination mode depicted as mode II in Scheme 1. The remaining two coordination sites around Mn1 are taken up by the oxygen terminals O21′′ [(′′): 2 – *x*, –0.5 + *y*, 1 – *z*] and O2′′′ [(′′′): –1 + *x*, *y*, *z*] of the quinate ligands belonging to two abutting Mn^{II} ions in the lattice

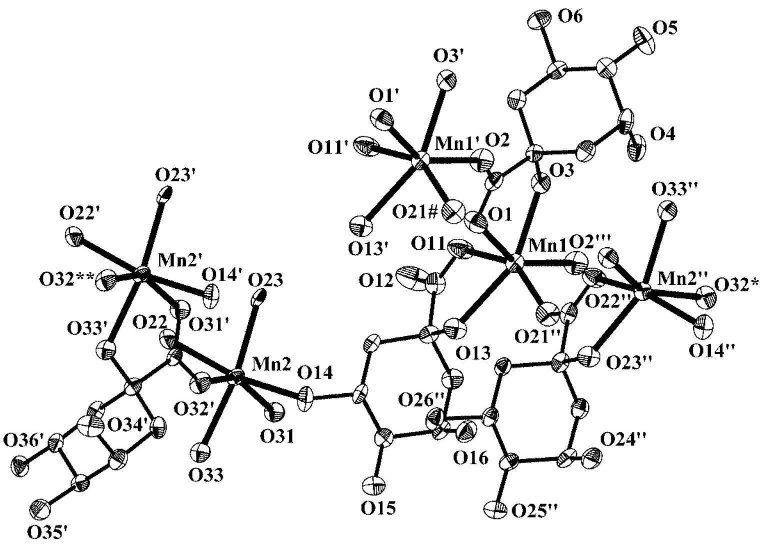

Figure 1. The molecular structure of $[Mn_2(C_7H_{11}O_6)_4]_n{\cdot}nH_2O$ (**1**) with the atom labeling scheme (50% thermal probability ellipsoids). Symmetry operations shown: ('): 1 + *x*, *y*, *z*; (''): 2 – *x*, –0.5 + *y*, 1 – *z*; ('''): –1 + *x*, *y*, *z*; (*): 1 – *x*, –0.5 + *y*, 1 – *z*; (**): 2 + *x*, *y*, *z*; (#): 3 – *x*, –0.5 + *y*, 1 – *z*.

{Mn2'' [(''): 2 – *x*, –0.5 + *y*, 1 – *z*] and Mn1''' [('''): –1 + *x*, *y*, *z*], respectively}. Collectively, the assembly of the aforementioned quinate ligands render the Mn1 ion six-coordinate with distorted octahedral geometry. In this octahedron, the terminal oxygens O1, O11, O21'', and O2''' define the equatorial plane, while the two remaining oxygens O3 and O13 occupy the axial positions.

A different type of coordination sphere is formulated around a second distinct manganese ion in the lattice. In particular, four coordination sites are taken up by two quinate ligands, both of which bind the manganese ion Mn2 through the carboxylate and alcohol oxygen terminals. These oxygen anchors are O31, O33 and O22, O23 for the corresponding carboxylate and alcohol oxygen terminals. One coordination site is occupied by the oxygen terminal

Scheme 1.

Table 1. Bond lengths [Å] and angles [°] in **1**.[a]

Lengths			
Mn1–O21''	2.067(4)	Mn2–O32'	2.104(4)
Mn1–O2'''	2.132(4)	Mn2–O31	2.132(4)
Mn1–O11	2.134(5)	Mn2–O22	2.142(4)
Mn1–O1	2.178(4)	Mn2–O33	2.202(4)
Mn1–O3	2.199(4)	Mn2–O23	2.216(5)
Mn1–O13	2.324(4)	Mn2–O14	2.314(4)
Angles			
O21''–Mn1–O2'''	96.75(17)	O32'–Mn2–O31	149.62(15)
O21''–Mn1–O11	148.53(17)	O32'–Mn2–O22	88.94(17)
O2'''–Mn1–O11	90.58(19)	O31–Mn2–O22	108.90(17)
O21''–Mn1–O1	92.25(18)	O32'–Mn2–O33	81.82(15)
O2'''–Mn1–O1	146.94(16)	O31–Mn2–O33	73.55(13)
O11–Mn1–O1	98.1(2)	O22–Mn2–O33	91.54(15)
O21''–Mn1–O3	119.46(16)	O32'–Mn2–O23	113.60(17)
O2'''–Mn1–O3	76.52(15)	O31–Mn2–O23	95.41(15)
O11–Mn1–O3	92.00(16)	O22–Mn2–O23	73.02(15)
O1–Mn1–O3	71.38(14)	O33–Mn2–O23	157.31(16)
O21''–Mn1–O13	80.11(16)	O32'–Mn2–O14	79.49(15)
O2'''–Mn1–O13	118.34(16)	O31–Mn2–O14	87.53(16)
O11–Mn1–O13	69.56(15)	O22–Mn2–O14	162.08(17)
O1–Mn1–O13	94.52(15)	O33–Mn2–O14	100.20(15)
O3–Mn1–O13	155.38(16)	O23–Mn2–O14	99.03(16)

[a] Symmetry transformations used to generate equivalent atoms: ('): 1 + *x*, *y*, *z*; (''): 2 – *x*, –0.5 + *y*, 1 – *z*; ('''): –1 + *x*, *y*, *z*.

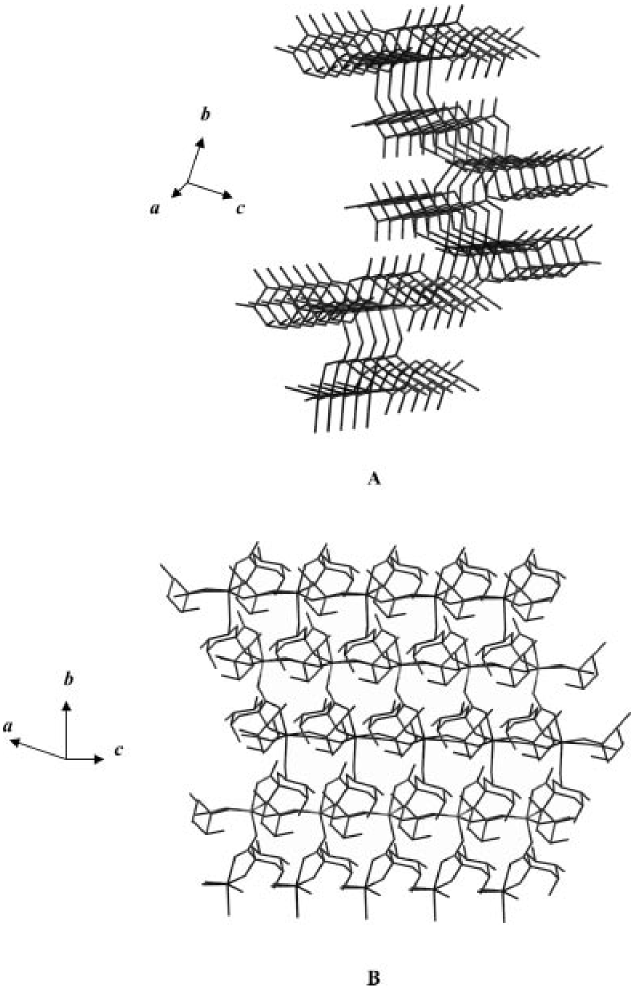

Figure 2. **A**: Packing diagram showing the chains of the Mn1 and Mn2 assemblies in **1** along the *a* axis. **B**: Layer diagram showing the bridging between Mn1 and Mn2 assemblies of **1** along the *a* axis forming the 2D polymeric structure.

O32′ [(′): 1 + *x*, *y*, *z*] of the carboxylate group of an abutting quinate ligand attached to a nearby manganese ion Mn2′ [(′): 1 + *x*, *y*, *z*], leading to a Mn2···Mn2′ separation equal to 5.813(3) Å, which is the length of the *a* axis. As a result, polymeric chains of the Mn2 assemblies are formed which are parallel to the crystallographic *a* axis. The last coordination site is occupied by the oxygen atom of one of the three alcohol moieties borne by the quinate ligand, namely O14, which is anchored to the first discrete Mn1 site discussed earlier. Overall, the coordination number of the Mn2 site is six, and the arising environment is distorted octahedral. The oxygen terminals O22, O32′, O31, and O14 formulate the equatorial composition of the octahedron, whereas the alcohol oxygen atoms O23 and O33 fulfil the axial requirements of the Mn2 environment.

The four crystallographically independent quinate ligands are divided into two groups according to their coordination mode around the two Mn^{II} ions. The first group contains three members which anchor to Mn^{II} through the carboxylate and alcohol oxygen atoms (O1, O3, O22, O23, O31, O33). In particular, the first member of the group binds to Mn1, while the two remaining members bind to Mn2 assemblies. The second carboxylate oxygen atom in all three quinate ligands is attached to a neighboring Mn^{II} ion in a *syn,anti* binding mode. More specifically, O1, O2 and O31, O32 bridge Mn^{II} ions belonging to Mn1 and Mn2 assemblies, respectively, and are responsible for the formation of the Mn1 and Mn2 polymeric chains along the *a* axis, while O21, O22 bridge Mn1 and Mn2′′ [Mn1···Mn2′′ 5.758(3) Å] and are responsible for the linkage of the chains. The second group contains one quinate ligand, which is anchored to Mn1 through O11 and O13, in the same way as the quinate ligands of the first group. In this case, however, the carboxylate moiety is coordinated to the metal ion in an η^1 fashion, and the alcohol oxygen O14 is used as a bridge to Mn2. Thus, that particular quinate ligand is used as an extended bridge between the chains of the two Mn^{II} assemblies yielding an 8.065(11) Å separation between Mn1 and Mn2. In conclusion, the multifunctional nature of the crystallographically distinct quinate ligands and the way they extend into the coordination sphere of Mn^{II} ions, promoting various coordination modes, are responsible for the formation of the 2D polymeric structure of compound **1** (Figure 2). This structure becomes even more complicated when hydrogen-bonding interactions are taken into consideration for the assembly of the requisite network.

Variable coordination modes of carboxylate-bearing organic ligands were previously observed in the coordination sphere of other divalent metal ions like Cd^{II} and Pb^{II}. Representative examples of such complexes include $Cu^{I}(OOCCH_3)$,[9] and the physiological ligand citrate-containing complexes $[Cd(C_6H_6O_7)(H_2O)]_n$ (**2**),[10] $[Cd_3(C_6H_5O_7)_2(H_2O)_5]\cdot H_2O$ (**3**) and $(NH_4)[Cd(C_6H_5O_7)(H_2O)]\cdot H_2O$ (**4**), and $[Pb(C_6H_6O_7)]_n\cdot nH_2O$ (**5**).[11]

The Mn–O bond lengths for **1** are in the range from 2.067(4) to 2.324(4) Å, very similar to corresponding distances in complexes $(NH_4)_4[Mn^{II}(C_6H_5O_7)_2]$ (**6**),[12] $Mn^{II}(C_4H_4O_5)\cdot 3H_2O$ [2.111(2)–2.220(2) Å],[13] $Mn^{II}(C_7H_3NO_5)(H_2O)_2$ [2.124(3)–2.262(1) Å],[14] $Mn^{II}(C_2H_3O_3)_2\cdot 2H_2O$ [2.124(3)–2.225(3) Å],[15] $[Mn^{II}(XDK)(NO_3)(CH_3OH)_4(H_2O)_2](NO_3)$ [2.116(2)–2.345(2) Å][16] [H_2XDK = *m*-xylenediamine bis(Kemp's triacid imide)] and $[Mn^{II}(bpca)_2\{Mn^{II}(hfac)_2\}_2]$ [2.113(3)–2.190(2) Å],[17] [Hbpca = bis(2-pyridylcarbonyl)amine; Hhfac = hexafluoroacetylacetone], where oxygen-containing octahedral coordination is the predominant feature of the structure around the Mn^{II} ion. Also worth noting is the case of the polymeric material $[Mn^{II}(H_2O)_6][Mn^{II}(C_6H_5O_7)(H_2O)]_2\cdot 2H_2O$.[18] In this compound, the observed Mn–O distances between the tridentate citrate and Mn^{II} range from 2.123(2) to 2.224(2) Å and compare favorably with those seen in **1**. The octahedral Mn^{II} ion in **1** corresponds to other octahedral divalent metal ions like Zn^{II},[19] Cu^{II},[20] and Ni^{II}[21] in analogous octahedral species bearing citrates. The M–O distances observed in those complexes are in agreement with those seen in **1** and range from 2.052(2) to 2.164(2) Å (Zn^{II}) and 2.021(3) to 2.072(3) Å (Ni^{II}), while a wider range due to Jahn–Teller distortions is observed in the copper analog [1.969(3)–2.341(3) Å]. Equally comparable are the M–O distances occurring in the congener quinate complexes $[Zn(C_7H_{11}O_6)_2]$,[22] $[Cd(C_7H_{11}O_6)_2]\cdot H_2O$, $[Cu(C_7H_{10}O_6)(H_2O)]_2\text{-}(H_2O)_2$,[23] $\{[Cu(NO_3)(C_7H_{11}O_6)(H_2O)]\cdot 2H_2O\}_n$, $\{[CuCl(C_7H_{11}O_6)(H_2O)]\cdot H_2O\}_n$,[24] $[Pt(C_6H_{14}N_2)(C_7H_{10}O_6)]$,[25] and the trinuclear $(NH_4)_2\{[V(O)_2]_2[V(O)](\mu\text{-}C_7H_{10}O_6)_2\}\cdot H_2O$.[26]

Overall, the quinate ligand plays the role of an efficient metal-ion chelator, employing all possible types of anchors available in its structure and effectively formulating the coordination environment around Mn^{II}.

Hydrogen-bonding interactions are a dominant feature of the crystal structure of **1**. Specifically in **1**, the alcohol and carboxylate moieties of the quinate ligands along with the lattice water molecules participate in an extensive network of intra- and intermolecular hydrogen bonds (Table 2), which very likely contributes to the stability of the crystal lattice.

Table 2. Hydrogen bonds in **1**.

Interaction	D···A [Å]	H···A [Å]	D–H···A [°]	Symmetry operation
O3–HO3···O4	2.663	1.891	155.3	*x*, *y*, *z*
O4–HO4···O36	2.793	1.980	166.1	1 – *x*, –0.5 + *y*, 1 – *z*
O5–HO5···O26	2.955	2.115	157.2	2 – *x*, –0.5 + *y*, –*z*
O6–HO6···O15	2.769	1.786	151.1	1 + *x*, *y*, –1 + *z*
O13–HO13···O16	2.704	1.963	142.9	*x*, *y*, *z*
O14–HO14···O6	2.725	1.820	169.8	*x*, *y*, 1 + *z*
O15–HO15···O5	2.831	2.001	145.2	*x*, *y*, 1 + *z*
O16–HO16···O26	2.872	2.098	177.9	1 – *x*, –0.5 + *y*, 1 – *z*
O23–HO23···O24	2.667	2.017	148.5	*x*, *y*, *z*
O24–HO24···O12	2.768	1.917	123.3	1 + *x*, *y*, *z*
O25–HO25···O35	2.740	1.904	169.4	*x*, *y*, –1 + *z*
O26–HO26···O36	2.919	2.162	159.9	*x*, *y*, –1 + *z*
O33–HO33···O34	2.648	1.962	146.5	*x*, *y*, *z*
O34–HO34···OW1	2.719	1.719	166.5	1 + *x*, *y*, 1 + *z*
O35–HO35···O12	2.683	1.800	162.2	*x*, *y*, 1 + *z*
O36–HO36···O25	2.781	1.831	164.1	–1 + *x*, *y*, 1 + *z*
OW1–HW1A···O12	2.960	2.282	143.7	*x*, *y*, *z*
OW1–HW1B···O11	2.908	1.959	167.4	–1 + *x*, *y*, *z*

FTIR Spectroscopy

The FTIR spectrum of **1** exhibits strong absorptions for the carbonyl groups of the carboxylate groups in both the antisymmetric and symmetric vibration regions. The antisymmetric stretching vibrations $\nu_{as}(COO^-)$ appear in the range 1639–1607 cm^{-1}, whereas the symmetric stretches $\nu_s(COO^-)$ appear in the range 1451–1380 cm^{-1}. The frequencies for the carbonyl stretches in **1** are shifted to lower values relative to those of the free quinic acid. Hence, they indicate a change in the vibrational status of the quinate anion upon coordination to the metal ion. The difference between the symmetric and antisymmetric stretches, $\Delta[\nu_{as}(COO^-) - \nu_s(COO^-)]$, is greater than 200 cm^{-1}, indicating that the carboxylate groups of the quinate ligand are either free or coordinated to the metal ion in a monodentate fashion.[9b,27] The latter contention is further confirmed by the X-ray crystal structure of **1**. Similar trends in the frequencies for the carboxylate carbonyl groups have also been observed in the FTIR spectra of other metal-quinate complexes as well as α-hydroxycarboxylate complexes with metal ions.[28]

Thermal Studies

The thermal decomposition of the title complex was studied by TGA-DSC under an atmosphere of oxygen. $[Mn_2(C_7H_{11}O_6)_4]_n\cdot nH_2O$ (**1**) is thermally stable up to 190 °C. From that point on, an initial process emerges that involves dehydration of **1**, with the release of water between 190 and 210 °C signifying an endothermic process. A fairly clear plateau is reached at 210 °C, suggesting that the arising anhydrous species is thermally stable. The observed weight loss, attributed to the release of the water content, amounts to 4.8 %, a value very close to the calculated value of 5.1 % based on the molecular formula of the title complex **1**.

Two additional steps are observed in the thermal decomposition of complex **1**. No clear plateaus are reached in these stages, suggesting that the derived products are unstable and decompose further. The total weight loss of 83 %, due to the decomposition of the title complex, is reached at 450 °C with no further loss up to 1000 °C. This value is in agreement with the calculated weight loss of 83 %, derived upon the proposition that the final product at 1000 °C is Mn_3O_4. The DSC profile of the complex exhibits clear features that correspond to the TGA diagram. Collectively, the rather small number of observed TGA and DSC peaks likely reflects simple mechanisms of decomposition pathways for the title complex.

Magnetic Susceptibility

The temperature dependence of χ_M and $\chi_M T$ (χ_M being the magnetic susceptibility for two Mn^{II} ions) for complex **1** is shown in Figure 3. The $\chi_M T$ value is 8.5 $emu\,mol^{-1}\,K$ at 300 K (close to the value expected for two isolated Mn^{II} ions). From 300 K down to 50 K there is a smooth decrease of the $\chi_M T$ value (Figure 3, A), while from 50 K down to 2 K there is a more pronounced decline of the $\chi_M T$ ultimately reaching the value of 1.5 $emu\,mol^{-1}\,K$. In the inset of Figure 3 (A), the maximum of the χ_M data is shown at 3.5 K. The shape of these curves is characteristic of the occurrence of weak antiferromagnetic interactions between the Mn^{II} centers. Taking into account the 2D character of **1**, the susceptibility data were fitted through the following approaches:

(a) The first one was based on the expansion series[29] of Lines for a $S = 5/2$ antiferromagnetic quadratic layer, riding on the exchange Hamiltonian $\boldsymbol{H} = \sum_{nn} J\boldsymbol{S_i}\cdot\boldsymbol{S_j}$, where $\sum_{nn}$ runs over all pairs of nearest-neighbor spins i and j [Equation (1)], in which $\theta = kT/|J|S(S+1)$ $C_1 = 4$, $C_2 = 1.448$, $C_3 = 0.228$, $C_4 = 0.262$, $C_5 = 0.119$, $C_6 = 0.017$, and N, g, and β have their usual meanings.

$$\frac{Ng^2\beta^2}{\chi|J|} = 3\theta + \left(\sum \frac{C_n}{\theta^{n-1}}\right) \tag{1}$$

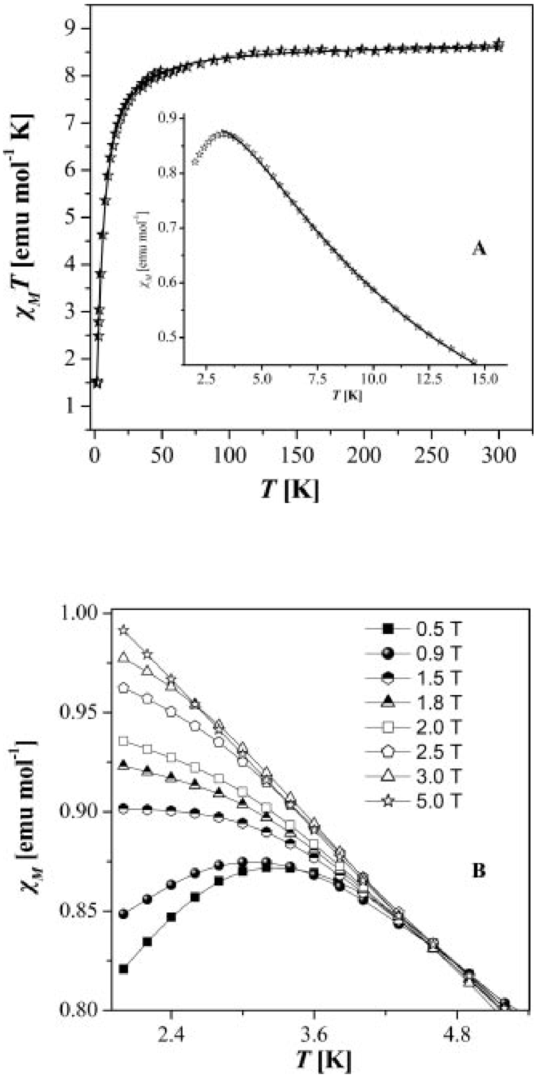

Figure 3. **A**: Temperature dependence of the susceptibility data at 0.6 T, in the form of $\chi_M T$ vs. T (solid stars). In the inset, the temperature dependence of the susceptibility data is shown at 0.6 T, in the form of χ_M vs. T near the maximum. The solid line represents the best fit according to the model discussed in the magnetic susceptibility section. **B**: Temperature dependence of the susceptibility data at different external fields in the range 0.5–5 T. The solid line represents the best fit according to the model discussed in the text.

The best fit is given by the superexchange parameters $J = -0.28\ \text{cm}^{-1}$ and $g = 1.98$. In this hypothesis, a quadratic character of the layer has been assumed, that is, only one J value. In fact, in complex **1** there are two J values because there are two chemically distinct pathways: The first coupling pathway involves pairs of abutting Mn^{II} ions, with the intervening linker emanating from a specific Mn^{II} ion and traversing through the α-hydroxycarboxylate moiety, the quinate cyclic backbone, and the terminal alcohol anchor, ultimately binding the abutting Mn^{II} ion. The second coupling pathway involves adjacent Mn^{II} ions with the shorter spacer linker being the α-hydroxycarboxylate moiety. The two distinct pathways in the *ab* plane are explicitly portrayed in Figure 4, with the appropriate schematic and the associated J (J_1 and J_2) coupling constants. As indicated earlier, both cases give a weak antiferromagnetic coupling, which we can assume to be similar for the fit.

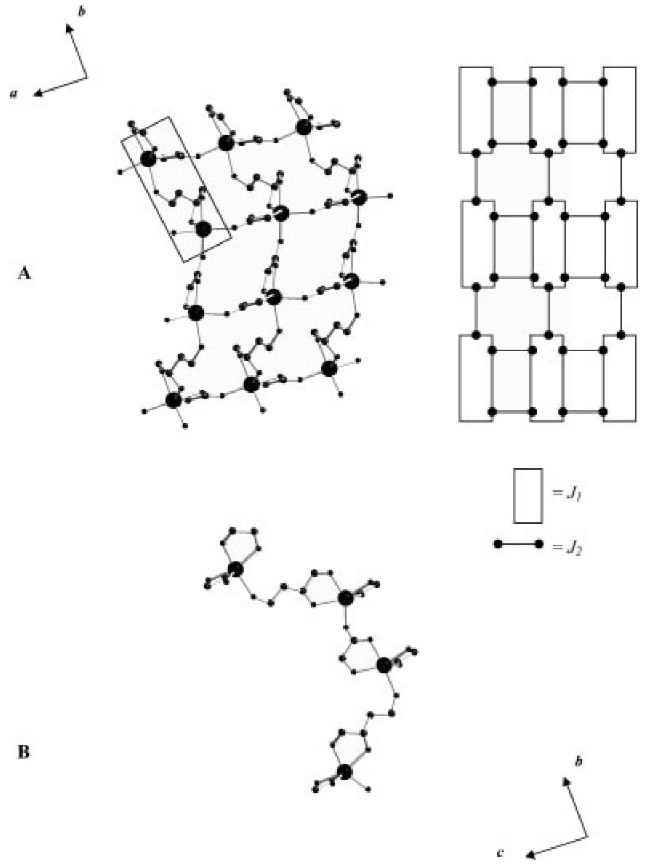

Figure 4. Different views (**A** and **B**) of the magnetic pathways of the system in **1**.

(b) The second one involved the analytical expression, derived by Curely, for an infinite 2D square lattice composed of classical spins ($S = 5/2$) isotropically coupled and based on the exchange Hamiltonian $\boldsymbol{H} = \sum_{nn} \boldsymbol{J S_i \cdot S_j}$, where $\sum_{nn}$ runs over all pairs of nearest-neighbor spins i and j (Heisenberg couplings), see Equation (2).[30]

$$\chi = \frac{\left[Ng^2\beta^2 S(S+1)(1+u)^2\right]}{\left[3kT(1-u)^2\right]} \qquad (2)$$

Here, N is Avogadro's number, β is Bohr's magneton, k is Boltzmann's constant, and u is the well-known Langevin function, see Equation (3).

$$u = L\left(\frac{JS(S+1)}{kT}\right) = \coth\left(\frac{JS(S+1)}{kT}\right) - \frac{kT}{JS(S+1)} \qquad (3)$$

The best fit leads to $J = -0.2\ \text{cm}^{-1}$ and $g = 1.98$ (Figure 3, part A, solid line). The J values obtained through the Lines or Curely expressions are very similar: –0.28 and –0.2 cm^{-1}, respectively. Taking into consideration the fact that the Curely formula is more accurate and is valid down to 0 K (the Lines formula is only valid up to the maximum of χ_M, approximately), the value of –0.2 cm^{-1} seems to be the most accurate estimate for complex **1**.

(c) Another possible magnetic model could also be considered. Such a model takes into account the fact that the only significant and maybe measurable interaction is the one through the α-hydroxycarboxylate ligand, thus reflecting a potential 1D character for **1**. For that reason, the susceptibility data were fitted to the following Equation (4),

$$\chi_M = \frac{Ng^2\beta^2}{kT}\frac{\left(A+Bx^2\right)}{\left(1+Cx+Dx^3\right)} \tag{4}$$

which is based on Weng's numerical approach,[31] and the coefficients have been generated by Hatfield et al.[32] for a $S = 5/2$ antiferromagnetic linear chain, where $x = |J|/kT$, $A = 2.9167$, $B = 208.04$, $C = 15.543$, $D = 2707.2$, and N, g, and β have their usual meanings. The best fit is given by the parameters $J = -0.2$ cm^{-1} and $g = 2.0$, and it is equally good, indicating that the couplings are weak. The distinction between a 2D and 1D magnetic model is quite difficult to address solely through the fitting of the susceptibility data. In order to investigate and confirm the 2D magnetic character of the system, a different experimental approach was employed and it is explained later.

The comparison of χ_M (note that here the quantity actually measured is the ratio between the magnetization and the applied magnetic field) versus T curves at different magnetic fields from 0.5 to 5.0 T applied fields (Figure 3, B) provides additional information. At the lower field, a clear sign of a transition to an antiferromagnetic state is observed with a maximum at 3.5 K. The critical temperature, taken as the maximum of the $T\mathrm{d}\chi/\mathrm{d}T$ versus T curve, was estimated to occur at 2.0 K.[33] On the other hand, no maximum is observed at 5 T, thus indicating that the transition is suppressed at this field. Interestingly, ZFC/FC curves measured at 50 G (not shown) did not reveal any divergence, thus indicating that no hysteretic phenomenon is active below the ordering temperature.

Isothermal magnetization curves at $T = 2$–5 K in the applied field 0–5 T are shown in Figure 5 (A). The curves for the increasing and decreasing fields are identical. The magnetization at 5 T reaches 8.4 and 6.8 μ_B at $T = 2$ and 5 K, respectively, values which are smaller than the expected saturation value of 10 μ_B (two isolated Mn^{II} ions) for the molecule of **1**. The sigmoidal shape of the $M(H)$ dependence is shown in Figure 5 (B), where a pronounced peak appears in the d$M(H)$/dH curve that disappears at temperatures higher than 5 K.[34] This shape reveals the metamagnetic-like behavioral characteristic for systems in which the magnetocrystalline anisotropy is superimposed on the exchange couplings. Similar features have been recently observed for Cu^{II}–W^{V} coordination polymers with 2D structures.[35] The shape of the $T = 2$ K curve suggests that the effective anisotropy field (H_A) is less than the exchange field (H_E), in contrast to the case of metamagnets, where $H_A \geq H_E$ and an immediate *spin-flip* transition to the saturated ferromagnetic state occurs. When the anisotropy field is of moderate intensity, the magnetization process proceeds through the *spin-flop* transition connected with reorientation of the antiferromagnetically coupled spins to the configuration perpendicular to the field. The threshold field for the spin-flop transition in the polycrystalline sample is 0.3 T, whereas the inflection point of the d$M(H)$/dH curve (Figure 5, B) occurs at $H_{SF} = 2.1$ T. At $T = 5$ K, the $M(H)$ curve hardly shows any transition, most probably because of the change of the H_A/H_E ratio.[36]

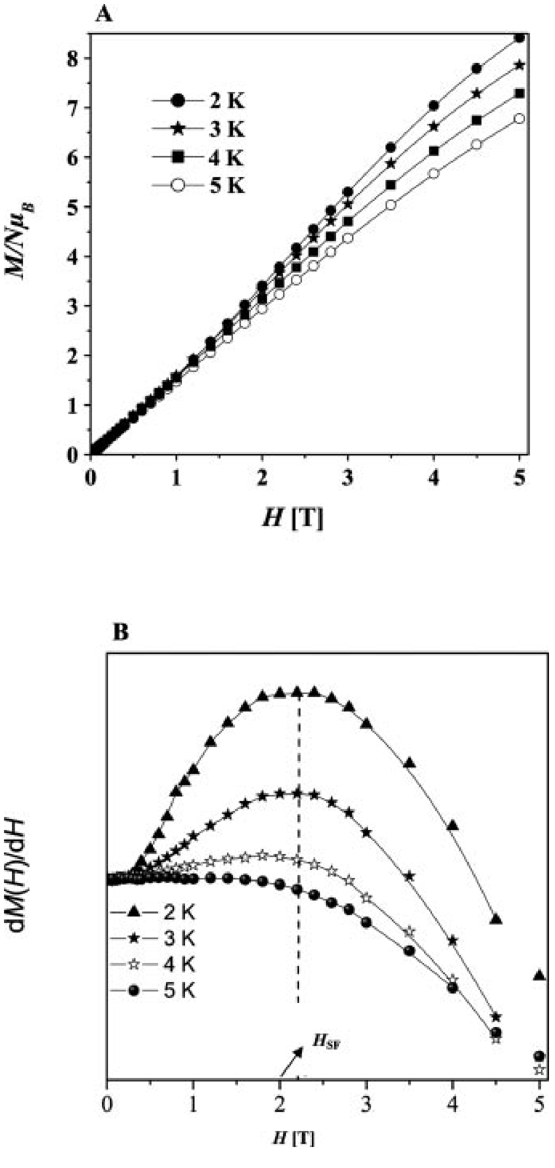

Figure 5. **A**: Magnetization curves at different temperatures in the field range 0–5 T. **B**: Field dependence of the magnetization derivatives in order to reveal their sigmoidal character (see text for details).

EPR Spectroscopy

The EPR spectrum of complex **1** measured on a polycrystalline powder at room temperature shows an isotropic signal centered at $g = 2.00$, with a line width of 380 G. The spectra measured at variable temperatures are practically identical, but the line width of the signal increases upon lowering of the temperature (at 4 K it is 650 G). Since the EPR signal does not vanish at low temperatures, proof for antiferromagnetic ordering below the temperature of the transition, the possible magnetic ordering, needs further measurements at a lower temperature (about 2 K, see earlier).

The Binary Mn^{II}-Quinate System in Aqueous Media

The synthesis of $[Mn_2(C_7H_{11}O_6)_4]_n \cdot nH_2O$ (**1**) through a facile reaction of $MnCl_2$ with quinic acid at pH 3, demonstrates the strong affinity of D-(–)-quinic acid for the divalent metal ion Mn^{II}. Albeit low, the pH of the reaction solution was sufficient to promote the reaction to completion and to afford the crystalline product in a pure form in a few hours. The physicochemical characterization of the derived material reflected the physical and chemical properties of **1** and revealed a considerable number of structural details linked to the reactivity of the binary system investigated. Specifically, the points worth noting are the following:

(a) *the retention of the protonation of the α-hydroxy group in the quinate ligand*. It appears that in the presence of Mn^{II}, the alcohol group adjacent to the carboxylic acid moiety retains its proton, following binding of the quinate group to the metal ion. Protonation of the alcohol group in the α position to the carboxylate group has also been observed in the case of the congener α-hydroxycarboxylic acid, citric acid, upon binding of the latter to Mn^{II}.[12]

(b) *employment of the terminal alcohol moieties in the coordination of the quinate ligand to an adjacently located Mn^{II} ion*. In that respect, the organic moiety extends its coordination to two distinct manganese ions by (1) employing different anchors to bind them, (2) satisfying the coordination requirements of both Mn^{II} ions, (3) preserving the protonation state of the alcohol group(s) upon binding to the metal ions, and (4) retaining the overall (de)protonation state of the carboxylate ligand bound to the manganese ion(s) to –1.

(c) *the variable mode of binding of the quinate carboxylate group to the Mn^{II} ions*. Here, there exist two coordination modes, one of which is the conventional mode and is often observed in the case of other metal ions bound to carboxylate-containing substrates. The second one is a characteristic coordination-binding motif (Scheme 1). In this sense, the two Mn^{II} ions to which the carboxylate group spans lie in the *syn-anti* conformation. This distinct mode of coordination has been observed for other metal ions bound to carboxylate-bearing molecules.[37] The two manganese ions lie in the same plane with carboxylate oxygen atoms and the abutting carbon atoms (the atoms, C1, C2, O1, O2, of the quinate backbone, Mn1, and Mn1′ are coplanar with the largest standard deviation 0.18 Å for O2).

The aforementioned structural features define the physical formulation of complex **1** and reflect the chemical reactivity, due to which the title species arose out of the reaction mixture and crystallized out of solution. The distinct modes of binding of the quinate ligand to the Mn^{II} ions led inevitably to the formulation of a dimeric assembly $Mn_2(C_7H_{11}O_6)_4$ in **1**. The latter moiety is the repeat unit of the polymeric compound **1**. To this end, species **1** is a polymer similar to the one in the previously reported polymeric manganese complex $[Mn^{II}(H_2O)_6][Mn^{II}(C_6H_5O_7)(H_2O)]_2 \cdot 2H_2O$. Despite the obvious differences between the fundamental ligands bound to the Mn^{II} in the two different complexes, (a) the underlying variability in the coordination mode of the two ligands to Mn^{II} and (b) the resulting geometric features with the associated total variable charges, signify the diversity of the chemical reactivity of the Mn^{II} ions towards α-hydroxycarboxylate ligands differing in their structure. In this case, the structural differences in the organic ligands reflect commensurate structural differences in the metal complexes in the two polymeric species. Such profoundly different chemical reactivity and structural variability may reflect analogously variable chemical reactivity at the biological level, where the two organic ligands constitute key molecular targets of essential biosynthetic pathways linked to cellular integrity and survival in bacteria and plants.

Further structural characteristics inherent to the lattice of **1** include the involvement of water molecules in the assembly. To that end, solvent water molecules of crystallization participate in the establishment of extensive hydrogen-bonding interactions throughout the lattice of **1**.

Mn^{II} Aqueous Speciation in Plants and Plant Fluids

Manganese is widely found in various structures and compartments in plants (e.g., older leaves, the plant stem, etc.),[38,39] contributing to their physiology.[40] Given that any influence of cellular biochemical processes entail bioavailable and thus soluble forms of manganese ions, Mn^{II} bound to quinic acid presents a distinct form of an essential ion promoting binary and ternary interactions in biological fluids. Akin to this notion is the fact that solubility of Mn^{II} increases at low pH, that is, under conditions employed in this work.[41] It is through such interactions that (bio)chemical reactivity arises, similar to the one linked to enzymes in the shikimate pathway in plants.[42] Of the variety of species that might form in solution, compound **1**, albeit insoluble itself, illustrates multimodal interactions of quinic acid with Mn^{II} at low pH. In this sense, the dinuclear core species in **1**, is only one of the various forms potentially arising in the aqueous milieu. Undoubtedly, a solution speciation study would help delineate the nature and properties of species forming as a function of pH and metal-ligand stoichiometry.

Furthermore, the chemical reactivity of the binary system studied here exemplifies one more aspect of the chemistry unfolding at the biological level, that is, the ability of the cell to seek and identify micronutrients influencing its physiology. In that respect, aqueous Mn^{II}-quinate species at low pH provide a first glimpse of the chemistry promoted by bacterial organisms to (a) internalize, and/or (b) metabolize organic substrates in the presence of Mn^{II}, and/or (c) bind substrates in the presence of toxic metal ions (e.g., Cd^{II}), thus inhibiting their metabolic processing.[43,44] Such chemistries could arise from the needs of a plant under variable environmental adversities (e.g., nutritional deficiencies, extreme changes in soil pH, accumulation of toxic metals and substrates, etc.).[45]

Mn^{II}-Containing Lattices in Mn^{II}-Organic Hybrid Materials

The lattice in **1** indicates the diversity of structural motifs generated by a single polydentate ligand: D-(–)-quinic acid gives rise to distinct Mn^{II} sites, binding to it through the hydroxy carboxylate groups on one hand and the triol moieties on the other. The 1D wires strewn along the *a* axis formulate a 2D lattice with gaps in between the Mn^{II}-quinate strings that potentially allow for variable chemical reactivity in the intervening space (Figure 2). In those strings, the octahedrality of Mn^{II} sites is a feature previously observed in $[Zn(C_7H_{11}O_6)_2]$, but not in $[Cd(C_7H_{11}O_6)_2]\cdot H_2O$, where a monocapped trigonal prismatic arrangement of quinates around Cd^{II} dictates a different lattice. Equally interesting is $[Cu(C_7H_{10}O_6)(H_2O)]_2(H_2O)_2$, where the lattice is dictated by the square pyramidal geometry around Cu^{II}. Even more complex appears to be the 3D Mn^{II}–citrate lattices of various species, like $[NaMn(C_6H_5O_7)]$ and $[Ca_2Mn(C_6H_5O_7)_2(H_2O)_4]_n$.[46] This plethora of lattice types involving variable structure ligands bearing similarity to quinic acid, project an equally diverse type of hybrid materials still eluding isolation and characterization under speciation conditions in binary and even ternary systems.

Conclusions

Collectively, the work on the binary Mn^{II}-quinic system of **1** (a) projects a clear view of the complexity of the speciation in aqueous media and the diversity of interactions developing in plant fluids, (b) sheds light on specific structural features of the related solid-state lattices that could be useful in designing new Mn^{II}-organic hybrid materials, and (c) defines the challenges of the future in the bioinorganic chemistry of quinic acid.

Experimental Section

Materials and Methods: All manipulations were carried out in the open air. $MnCl_2\cdot 4H_2O$ was purchased from Merck and D-(–)-quinic acid from Fluka. Nanopure-quality water was used for all reactions.

Physical Measurements: FTIR measurements were recorded with a 1760X FT-Infra Red spectrometer from Perkin–Elmer, using KBr pellets. A ThermoFinnigan Flash EA 1112 CHNS elemental analyzer was used for the simultaneous determination of carbon, hydrogen, and nitrogen (%). The analyzer was based on the dynamic flash combustion of the sample (at 1800 °C) followed by reduction, trapping, complete GC separation and detection of the products. The instrument was fully automated and controlled by PC using the Eager 300 dedicated software and was capable of handling solid, liquid or gaseous substances.

A TA Instruments thermal analyzer, model Q 600, system was used to run the simultaneous TGA-DSC experiments. The employed heating rate was 10 °C min^{-1}. The instrument mass precision was 0.1 µg. Sample (about 20 mg) was placed in an open alumina sample pan for each experiment. High purity helium and air (80:20 in N_2/O_2) were used at a constant flow rate of 100 mL min^{-1}, depending on the conditions required for running the experiment(s). During the experiments, the sample weight loss and rate of weight loss were recorded continuously under dynamic conditions, as a function of time or temp., in the range 30–1000 °C. Prior to activating the heating routine program, the entire system was purged with the appropriate gas for 10 min, at a rate 400 mL min^{-1}, to ensure that the desired environment was established.

The EPR spectra of complex **1** in the solid state and in aqueous solutions were recorded with a Bruker ER 200D-SRC X-band spectrometer, equipped with an Oxford ESR 9 cryostat at 9.174 GHz, 10 dB, and at 4 K. Magnetic susceptibility data were collected using powdered samples of **1** with a Quantum Design SQUID susceptometer in the 2–300 K temp. range, under various applied magnetic fields. Magnetization measurements were carried out at three different temp. in the field range 0.5–5 T.

Synthesis of $[Mn_2(C_7H_{11}O_6)_4]_n\cdot nH_2O$ (1): $MnCl_2\cdot 4H_2O$ (0.50 g, 2.5 mmol) and D-(–)-quinic acid (0.97 g, 5.0 mmol) were placed in a round-bottomed flask (25 mL) and dissolved in water (5 mL). The reaction mixture was then stirred at room temp. until both reactants were completely dissolved. Subsequently, the pH of the clear solution was adjusted to 3 with aqueous ammonia. The resulting reaction mixture was allowed to stand at room temp. for slow evaporation. A few hours later, colorless crystalline material appeared on the bottom of the flask. The crystalline product was isolated by filtration and dried in vacuo. Yield 0.56 g (50%). **1**, $[Mn_2(C_7H_{11}O_6)_4]_n\cdot nH_2O$, $C_{28}H_{46}Mn_2O_{25}$ (892.52): calcd. C 37.64, H 5.15; found C 37.39, H 5.09.

X-ray Crystal Structure Determination: X-ray quality crystals of compound **1** (Table 3) were grown from reaction mixtures upon slow evaporation. A single crystal with dimensions 0.50 × 0.30 × 0.20 mm (**1**) was mounted on a $P2_1$ Nicolet diffractometer using graphite monochromated Cu-K_α radiation. Unit cell dimensions for **1** were determined and refined by using the angular settings of 25 automatically centered reflections in the range $22 < 2\theta < 54°$. Relevant crystallographic data appear in Table 3. Intensity data were measured by using a θ-2θ scan. Three standard reflections were monitored every 97 reflections, over the course of data collection. They showed less than 3% variation and no decay. Lorentz, polarization, and psi-scan absorption corrections were applied using Crystal Logic software. Further crystallographic details for **1**: $2\theta_{max} = 118°$; scan speed 3.0° min^{-1}; scan range $2.45 + a_1a_2$ separation; reflections collected/unique/used, 4667/4467[$R_{int} = 0.0372$]/4467; 620 parameters refined; $[\Delta/\sigma]_{max} = 0.018$; Flack parameter = 0.023(5); $[\Delta\rho]_{max}/[\Delta\rho]_{min}$ = 0.312/–0.639 e Å^{-3}; R/R_w (for all data) = 0.0506/0.1140. The structure of compound **1** was solved by direct methods using SHELXS-86[47] and refined by full-matrix least-squares techniques on F^2 by using SHELXL-97.[48] All the non-hydrogen atoms were refined anisotropically. The methylene hydrogen atoms of the quinate ligand were introduced at calculated positions as riding on bonded atoms. The remainder of the hydrogen atoms were located by difference Fourier maps and were refined isotropically.

Table 3. Summary of crystal, intensity collection, and refinement data for $[Mn_2(C_7H_{11}O_6)_4]_n \cdot nH_2O$ (**1**).

Formula	$C_{28}H_{46}Mn_2O_{25}$
Formula weight	892.52
T [K]	298
Wavelength	Cu-K_α 1.5480
Space group	$P2_1$
a [Å]	5.813(3)
b [Å]	21.72(1)
c [Å]	13.334(8)
β [°]	93.17(2)
V [Å^3]	1681.0(15)
Z	2
$D_{calcd.}/D_{measd.}$ [Mg m^{-3}]	1.763/1.77
Absorption coeff. (μ) [mm^{-1}]	7.061
Range of h, k, l	–6 to 6, –24 to 23, –14 to 0
Goodness-of-fit on F^2	1.031
R indices[a]	R = 0.0440, R_w = 0.1085[b]

[a] R values are based on F values, R_w values are based on F^2. $R = \frac{\sum \left||F_o| - |F_c|\right|}{\sum(|F_o|)}$, $R_w = \sqrt{\sum\left[w(F_o^2 - F_c^2)^2\right] / \sum\left[w(F_o^2)^2\right]}$. [b] For 4058 reflections with $I > 2\sigma(I)$.

CCDC-290297 (for **1**) contains the supplementary crystallographic data for this paper. These data can be obtained free of charge from The Cambridge Crystallographic Data Centre via www.ccdc.cam.ac.uk/data_request/cif.

Acknowledgments

This work was supported with funds provided by the Department of Chemical Engineering, Aristotle University of Thessaloniki. A.S. would like to acknowledge the financial support to this project by a "Pythagoras" grant from the National Ministry of Education and Religious Affairs and by a "PENED" grant from the General Secretariat of Research and Technology, Greece.

---

[1] P. Chappuis, J. Poupon, J. Arnaud, in *Trace Elements and Free Radicals in Oxidative Diseases* (Eds.: A. E. Favier, J. Neve, P. Faure), AOCS Press, Champaign, Illinois, **1994**, p. 46.

[2] a) C. D. Davis, J. L. Greger, *Am. J. Clin. Nutr.* **1992**, *55*, 747–752; b) L. L. Ji, F. W. Stratman, H. A. Lardy, *J. Am. Coll. Nutr.* **1992**, *11*, 79–86.

[3] a) J. E. Penner-Hahn, in *Manganese Redox Enzymes* (Ed.: V. L. Pecoraro), Verlag Chemie, New York, **1992**, p. 29; b) Y. Kono, I. Fridovich, *J. Biol. Chem.* **1983**, *258*, 13646–13648; c) Y. Kono, I. Fridovich, *J. Biol. Chem.* **1983**, *258*, 6015–6019; d) G. S. Allgood, J. J. Perry, *J. Bacteriol.* **1986**, *168*, 563–567; e) V. V. Barynin, A. Grebenko, *Dokl. Akad. Nauk U. S. S. R.* **1986**, *286*, 461.

[4] a) M. Aschner, in *Metals and Oxidative Damage in Neurological Disorders* (Ed.: J. R. Connor), Plenum Press, New York, **1997**, chapter 5, pp. 77–130; b) J. R. Prohaska, *Physiol. Rev.* **1987**, *67*, 858–901; c) F. C. Wedler, in *Progress in Medicinal Chemistry* (Eds.: G. P. Ellis, D. K. Luskombe), Elsevier Science, Amsterdam, **1993**, *30*, pp. 89–133.

[5] a) D. B. Calne, N. S. Chu, C. C. Huang, C. S. Lu, W. Olanow, *Neurology* **1994**, *44*, 1583–1586; b) S. E. Chia, S. C. Foo, S. L. Gan, J. Jeratnam, C. S. Tian, *Scand. J. Work Environ. Health* **1993**, *19*, 264–270; c) M. Florence, in *Proceeding on the Workshop on the Bioavailability and Oral Toxicity of Manganese* (Ed.: S. Velasquez), EPA Liaison, US EPA, **1995**, pp. 83–94.

[6] a) V. L. Pecoraro, in *Manganese Redox Enzymes* (Ed.: V. L. Pecoraro), Verlag Chemie, New York, **1992**; b) V. L. Pecoraro, M. J. Baldwin, A. Gelasco, *Chem. Rev.* **1994**, *94*, 807; c) G. C. Dismukes, *Chem. Rev.* **1996**, *96*, 2909; d) V. K. Yachandra, K. Sauer, M. P. Klein, *Chem. Rev.* **1996**, *96*, 2927.

[7] a) E. Haslam, *Shikimic Acid: Metabolism and Metabolites*, John Wiley & Sons, New York, **1993**; b) A. J. Pittard, in *Escherichia coli and Salmonella: Cellular and Molecular Biology* (Ed.: F. C. Neidhardt), ASM Press, Washington, DC, **1996**, chapter 28.

[8] R. Bentley, *Crit. Rev. Biochem. Mol. Biol.* **1990**, *25*, 307–384.

[9] a) R. D. Mounts, T. Ogura, Q. Fernando, *Inorg. Chem.* **1974**, *13*, 802–805; b) G. B. Deacon, R. Philips, *J. Coord. Chem. Rev.* **1980**, *33*, 227–250.

[10] M. Dakanali, E. T. Kefalas, C. P. Raptopoulou, A. Terzis, T. Mavromoustakos, A. Salifoglou, *Inorg. Chem.* **2003**, *42*, 2531–2537.

[11] M. Kourgiantakis, M. Matzapetakis, C. P. Raptopoulou, A. Terzis, A. Salifoglou, *Inorg. Chim. Acta* **2000**, *297*, 134–138.

[12] M. Matzapetakis, N. Karligiano, A. Bino, M. Dakanali, C. P. Raptopoulou, V. Tangoulis, A. Terzis, J. Giapintzakis, A. Salifoglou, *Inorg. Chem.* **2000**, *39*, 4044–4051.

[13] W. Van Havere, A. T. H. Lenstra, H. J. Geise, *Acta Crystallogr., Sect. B* **1980**, *36*, 3117–3120.

[14] L. C. Nathan, C. A. Doyle, A. M. Mooring, D. C. Zapien, S. K. Larsen, C. G. Pierpont, *Inorg. Chem.* **1985**, *24*, 2763–2766.

[15] T. Lis, *Acta Crystallogr., Sect. B* **1980**, *36*, 701–703.

[16] T. Tanase, S. J. Lippard, *Inorg. Chem.* **1995**, *34*, 4682–4690.

[17] T. Kajiwara, I. J. Tasuku, *J. Chem. Soc., Dalton Trans.* **1998**, 3351–3352.

[18] H. L. Carrell, H. P. Glusker, *Acta Crystallogr., Sect. B* **1973**, *29*, 638–640.

[19] R. Swanson, W. H. Ilsley, A. G. Stanislowski, *J. Inorg. Biochem.* **1983**, *18*, 187–194.

[20] R. C. Bott, D. S. Sagatys, D. E. Lynch, G. Smith, C. H. L. Kennard, T. C. W. Mak, *Aust. J. Chem.* **1991**, *44*, 1495–1498.

[21] Z.-H. Zhou, Y.-J. Lin, H.-B. Zhang, G.-D. Lin, K.-R. Tsai, *J. Coord. Chem.* **1997**, *42*, 131–141.

[22] Y. Inomata, T. Haneda, F. S. Howell, *J. Inorg. Biochem.* **1999**, *76*, 13–17.

[23] N. Barba-Behrens, F. Salazar-Garcia, A. M. Bello-Ramirez, E. Garcia-Baez, M. J. Rosales-Hoz, R. Contreras, A. Flores-Parra, *Trans. Met. Chem.* **1994**, *19*, 575.

[24] I. Bkouche-Walksman, *Acta Crystallogr., Sect. C* **1994**, *50*, 62.

[25] G. Hata, Y. Kitano, T. Kaneko, H. Kawai, M. Mutoh, *Chem. Pharm. Bull.* **1992**, *40*, 1604.

[26] R. Codd, T. W. Hambley, P. A. Lay, *Inorg. Chem.* **1995**, *34*, 877.

[27] C. Djordjevic, M. Lee, E. Sinn, *Inorg. Chem.* **1989**, *28*, 719–723.

[28] a) M. Matzapetakis, C. P. Raptopoulou, A. Tsohos, B. Papaefthymiou, N. Moon, A. Salifoglou, *J. Am. Chem. Soc.* **1998**, *120*, 13266–13267; b) M. Matzapetakis, C. P. Raptopoulou, A. Terzis, A. Lakatos, T. Kiss, A. Salifoglou, *Inorg. Chem.* **1999**, *38*, 618–619.

[29] a) M. E. Lines, *J. Phys. Chem. Solids* **1970**, *31*, 101; b) A. Escuer, R. Vicente, M. A. S. Goher, F. A. Mautner, *J. Chem. Soc., Dalton Trans.* **1997**, 4431 and references cited therein.

[30] a) J. Curely, *Europhys. Lett.* **1995**, *32*, 529; b) J. Curely, *Physica B* **1998**, *245*, 263; c) J. Curely, *Physica B* **1998**, *254*, 277; d) J. Curely, J. Rouch, *Physica B* **1998**, *254*, 298.

[31] C. H. Weng, Ph. D. Dissertation, Carnegie-Mellon University, Pittsburgh, PA, **1968**.

[32] W. Hiller, J. Strahle, A. Datz, M. Hanack, W. E. Hatfield, L. W. ter Haar, P. Gutlich, *J. Am. Chem. Soc.* **1984**, *106*, 329.

[33] M. E. Fisher, *Proc. R. Soc. (London) A* **1960**, *254*, 66.

[34] P. Przychodzen, K. Lewinski, M. Bałanda, R. Pełka, M. Rams, T. Wasiutynski, C. Guyard-Duhayon, B. Sieklucka, *Inorg. Chem.* **2004**, *43*, 2967.

[35] a) D.-F. Li, L. M. Zheng, X. Y. Wang, J. Huang, S. Gao, W. X. Tang, *Chem. Mater.* **2003**, *15*, 2094; b) S.-I. Ohkoshi, Y. Arimoto, T. Hozumi, H. Seino, Y. Mizobe, K. Hashimoto, *Chem. Commun.* **2003**, 2772.

[36] L. J. deJongh, A. R. Miedema, *Adv. Phys.* **1974**, *23*, 220.

[37] B.-H. Ye, X.-Y. Li, I. D. Williams, X.-M. Chen, *Inorg. Chem.* **2002**, *41*, 6426–6431.

[38] W. Hofner, *Physiol. Plant.* **1970**, *23*, 673.

[39] J. Vlamis, D. E. Williams, *Plant Sci.* **1973**, *39*, 245.

[40] F. Adams, J. I. Wear, *Soil Sci. Soc. Am. Proc.* **1957**, *21*, 305.

[41] G. H. Godo, H. M. Reisennauer, *Soil Sci. Soc. Am. J.* **1980**, *44*, 993.

[42] R. Entus, M. Poling, K. M. Herrmann, *Plant Physiology* **2002**, *129*, 1866–1871.

[43] A. J. Francis, C. J. Dodge, J. B. Gillow, *Nature* **1992**, *356*, 140–142.

[44] a) G. Joshi-Toppe, A. J. Francis, *J. Bacteriol.* **1995**, *177*, 1989–1993; b) L. Brynhildsen, T. Rosswall, *Appl. Env. Microbiol.* **1989**, *55*, 1375–1379.

[45] E. Hiltbrunner, W. Flückiger, *Tree Physiol.* **1996**, *16*, 963–975.

[46] W. Wang, X. Zhang, F. Chen, C. Ma, C. Chen, Q. Liu, D. Liao, L. Li, *Polyhedron* **2005**, in press.

[47] G. M. Sheldrick, *SHELXS-86: Structure Solving Program*, University of Göttingen, Germany, **1986**.

[48] G. M. Sheldrick, *SHELXL-97: Structure Refinement Program*, University of Göttingen, Germany, **1997**.

Received: December 6, 2005